Robust Aerial Object Tracking in Images with Lens Flare

Andreas Nussberger[1], Helmut Grabner[1] and Luc Van Gool[1]

***Abstract*— The goal of integrating drones into the civil airspace requires a technical system which robustly detects, tracks and finally avoids aerial objects. Electro-optical cameras have proven to be an adequate sensor to detect traffic, especially for smaller aircraft, gliders or paragliders. However the very challenging environmental conditions and image artifacts such as lens flares often result in a high number of false detections. Depending on the solar radiation lens flares are very common in aerial images and hard to distinguish from aerial objects on a collision course due to their similar size, shape, brightness and trajectories. In this paper we present an efficient method to detect lens flares within aerial images based on the position of the sun with respect to the observer. Using the date, time, position and attitude of the observer we predict the lens flare direction within the image. Once the direction is known the position, size and shape of the lens flares are extracted. Experiments show that our approach is able to compensate for errors in the parameters influencing the calculation of the lens flare direction. We further integrate the lens flare detection into an aerial object tracking framework. A detailed evaluation of the framework with and without lens flare filter shows that false tracks due to lens flares are successfully suppressed without degrading the overall tracking system performance.**

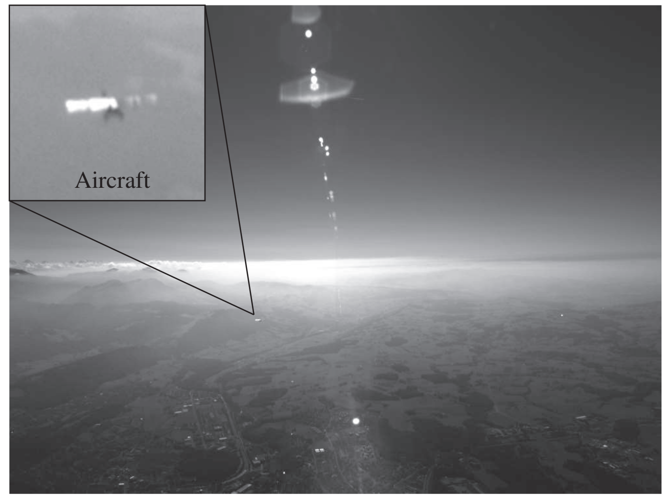

Fig. 1. Example image with lens flares taken from an airborne platform. In the upper left corner a magnified cutout of the traffic aircraft is shown - it looks similar to some of the lens flares in terms of its size, shape and brightness.

I. Introduction

The demand to operate Remotely Piloted Aircraft Systems (RPAS) in the civil airspace is continuously increasing. In 2013 the U.S. and Europe finally published particular roadmaps [1], [2] how to integrate RPAS into their national airspace - a result of years of work within different working groups. Besides all the open questions regarding regulations and certification of such systems there are also major technical challenges remaining. One of the biggest technical challenges to operate an RPAS beyond line of sight is to have an appropriate replacement of the pilot 'See and Avoid' capability on-board the RPAS, also known as 'Detect and Avoid'.

Over the last years a lot of research activities started with the focus on Detect and Avoid to evaluate sensors and algorithms which robustly detect and track aerial objects of different types [3]–[8]. Most of these projects use a RADAR and/or electro-optical (EO) cameras to detect aerial objects, especially for smaller airspace users, gliders and paragliders. Even though the presented results are promising, the available methods usually suffer from a high number of false detections due to the very challenging environmental conditions (e.g. ground clutter, lighting conditions, clouds). As a result of this, most approaches to detect aerial objects with EO sensors are limited to the sky region of an image. This is a strong limitation when flying within airspace classes where small airspace users are operating (usually at low altitude). The problem grows worse if the system is to be operated in a mountainous area.

This paper is based on previous work [7], where an experimental Detect and Avoid system was built up based on a custom sensor nose-pod mounted to a Diamond DA-42 aircraft. The sensor nose-pod has a built-in GPS receiver, an Inertial Measurement Unit (IMU), two high resolution 8 megapixel cameras, an ADS-B[1] and a FLARM[2] receiver. With this sensor-equipped Diamond aircraft and another traffic aircraft artificial collision scenarios were recorded. Based on this dataset an aerial object tracking framework able to detect aircraft against a background of sky and terrain was developed. That paper also introduced multiple filter steps to reduce false tracks due to ground clutter or static objects, e.g. dirt on the lens. One major issue with the presented implementation, however, is that image artifacts such as lens flares (see Figure 1 and 2) are critical candidates for false tracks and therefore significantly degrade system performance. This is the issue dealt with in this paper.

Lens flares are an artifact occurring in optical lens systems

*This work is supported by armasuisse Science and Technology, affiliated with the Swiss Federal Department of Defense, Civil Protection and Sport

[1]Andreas Nussberger, Helmut Grabner and Luc Van Gool are with the Computer Vision Laboratory, ETH Zurich, Switzerland {nussberger,grabner,vangool}@vision.ee.ethz.ch

[1]ADS-B is a standardized aviation technology to transmit the own GPS position and velocity to other airspace users. The maximum range is given by the transponder transmission power and can extend 100 km.

[2]FLARM is a proprietary traffic collision warning system with focus on general aviation and provides traffic warnings within a range of 3-5 km.

Fig. 2. Example aerial images with lens flare and blooming artifacts.

if light is internally reflected or scattered in between the optical elements [9, pp.123-133]. This usually happens if a bright light source is within or close to the camera field of view. The characteristics of the final artifacts heavily depend on the mechanical and optical properties of the lens system.

When the Detect and Avoid image dataset was captured, lenses covered by a special coating to suppress interreflections together with lens hoods were used. In addition, the windows in front of the cameras to protect the lenses in the custom nose-pod were also treated with an anti-reflective coating and the interior of the pod was painted in dull black. Still, lens flares are present in the images, as the examples have already shown. A detailed analysis of the presented dataset has shown that lens flares are present in at least one of the cameras in more than one-third of the scenarios. Their occurrence depends on the aircraft heading and the time of day and is a serious issue to consider for everyday operation of a camera-based Detect and Avoid system. As shown in Figure 1 the lens flares can be hard to distinguish from an aircraft on a collision course because of their similar size, shape and brightness. Even worse, these lens flares start moving around in the image if the position and/or attitude of the camera with respect to the light source is changed. Depending on the observer motion, these trajectories look similar to those of an approaching traffic aircraft.

Blooming, another artifact due to a bright light source shown on the right of Figure 2 is usually less of a problem because of its massive size which can easily be distinguished from a potential traffic aircraft.

In this paper we present a new method to efficiently detect lens flares within aerial images based on the position of the sun with respect to its observer. A detailed parameter evaluation of the lens flare detection shows the errors affecting the calculation of the lens flare direction and allows to demonstrate the robustness of the method regarding errors in the required meta information. Based on the detected lens flares we integrate an additional 'lens flare filter' into the aerial object tracking framework which allows us to successfully remove false tracks due to lens flares moving across the image. We will show improved results based on the same dataset as used in [7] and additional scenarios containing lens flares.

The paper is structured as follows. Section II introduces the lens flare detection including two approaches to detect the lens flare direction. In Section III we present a detailed evaluation of the proposed method based on a manually labeled dataset. Section IV shows experimental results for the lens flare detection applied to aerial object tracking, and in Section V we conclude the paper.

II. Lens Flare Detection

The identification of lens flares within an image is a nontrivial task to achieve if no additional information is available at all. When using high grade lens systems the lens flares are usually found close to a straight line connecting the position of the light source (the sun) and the optical center of the image. This is a result of the mechanical architecture of optical lens systems. The optical center of an image is identified by a camera calibration [10].

Our approach to identify lens flares within an (aerial) image as shown in Figure 1 is based on two steps which allows to keep computational costs low: first, the lens flare direction within the camera image is estimated. Second, based on the estimated lens flare direction a small subset of the original frame is processed and lens flares are extracted. The details of the two steps are explained in the following subsections.

A. Estimating the lens flare direction

Based on the assumption that lens flares lie close to a line through the optical center of the image we are able to limit the search region for lens flares considerably. Therefore we define the 'lens flare window' as a function of the lens flare direction α and the window width w (see Figure 3). The calculation of the lens flare window is based on the polar form of the line equation:

$$y = -\frac{\sin(\alpha)}{\cos(\alpha)} \cdot x + \frac{r}{\cos(\alpha)}, \text{with } r \in \left[-\frac{w}{2}, \frac{w}{2}\right]. \qquad (1)$$

An accurate estimate of the lens flare direction α is the key element to an efficient detection of lens flares within an image. With increasing accuracy of the estimated angle α, the window width w and therefore the number of pixels to be processed can be reduced significantly.

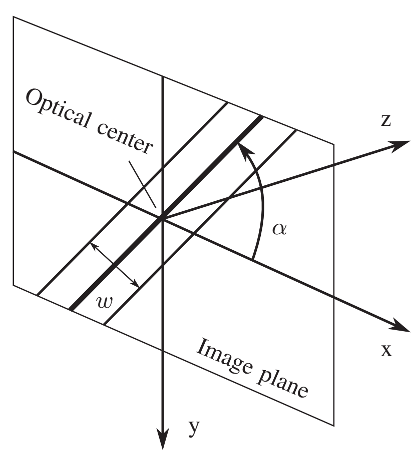

Fig. 3. The subset of an image to be searched for lens flares is defined as the 'lens flare window' given by the lens flare direction α and the window width w.

1) Calculating α without external information: The lens flare direction α is estimated without additional knowledge - just based on the assumption that lens flares lie in a lens flare window - as follows. We rotate the lens flare window ($w = const.$) across the image by sampling α at fixed steps $\Delta\alpha$ in the range of $[0, \pi]$. For every window the lens flare candidates are extracted as explained in Section II-B. The resulting estimated lens flare direction is given by the direction which provides the highest number of lens flare candidates. With this approach we are able to identify the correct lens flare direction within a large number of situations with the downside of the resulting computational costs due to the repeated execution of the lens flare extraction. See Section III for a detailed analysis.

2) Calculating α from the sun position: Another property of lens flares we did not consider in the previous approach is that their direction is going through the position of the light source. In this section we extend the previous method by taking this additional prior into account.

To calculate the position of the sun, we have to know the exact position and orientation of the observer (the camera) as well as the current date and time. The position, date and time of the camera are given by the GPS receiver. The camera orientation is available from the IMU attitude measurements. We use existing mathematical models from Astronomy (see [11], [12] and references therein) to calculate the azimuth and elevation angle of the sun with respect to the Navigation reference frame at the aircraft position. In the next step, we have to transform these angular values from the Navigation reference frame into the Camera reference frame as shown in Figure 4.

The transformation from the Navigation to the Camera reference frame includes two rotations and no translations, because we assume the origins for all three reference frames to coincide. The first rotation R_{BN} from Navigation to Body reference frame is given by the Euler angles ϕ, θ and ψ from the IMU:

$$R_{BN}(\phi,\theta,\psi) = R_{BN''}(\psi) \cdot R_{N''N'}(\theta) \cdot R_{N'N}(\phi)$$
$$= \begin{pmatrix} c_\theta c_\psi & c_\theta s_\psi & -s_\theta \\ -c_\phi s_\psi + s_\phi s_\theta c_\psi & c_\phi c_\psi + s_\phi s_\theta s_\psi & s_\phi c_\theta \\ s_\phi s_\psi + c_\phi s_\theta c_\psi & -s_\phi c_\psi + c_\phi s_\theta s_\psi & c_\phi c_\theta \end{pmatrix}, \quad (2)$$

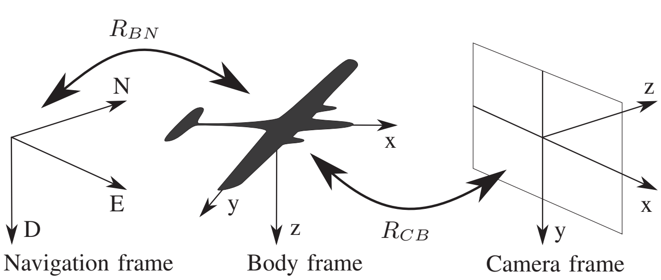

Fig. 4. The three reference frames used to map the global position of the sun into the Camera reference frame are as follows: the Navigation reference frame N on the left with global North-East-Down axis. The Body reference frame B attached to the aircraft, as shown in the middle. The Camera reference frame C located at the camera image center on the right.

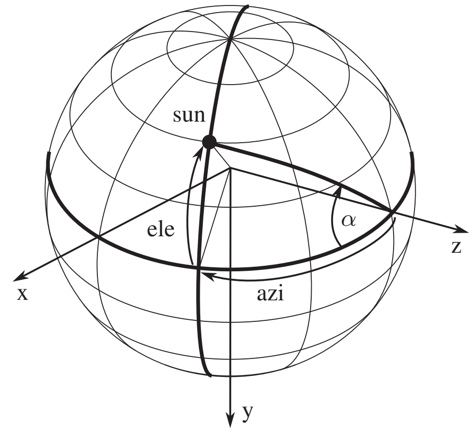

Fig. 5. The calculation of the lens flare direction angle α in the camera reference frame is based on the sun position azimuth and elevation angles.

where c_* and s_* are abbreviations for the cosine and sine of the corresponding angle. The second rotation R_{CB} from the Body to the Camera reference frame is given by the extrinsic camera calibration and is based on the same rotation matrix as R_{BN}.

Once the sun position azimuth and elevation angles are available in the Camera reference frame (see Figure 5), we can directly compute the lens flare direction α using Equation (3) given by spherical trigonometry.

$$\alpha = \arctan\left(\frac{\tan(ele)}{\sin(azi)}\right) \quad (3)$$

If one of the required meta signals to calculate the sun position is missing or invalid, we use the pure image-based approach presented above as fallback solution to get an approximate initial estimate for the lens flare direction α.

B. Extracting Lens Flares

For the aerial object tracking framework the simplest approach to remove lens flares would be to prevent detections within the lens flare window. However, this method would result in a constantly 'blind' area within the camera. By extracting the single flares we are able to correctly filter the few spots in the image which are continuously changing their size and position due to minor attitude changes even during level flight.

Based on the estimated lens flare direction α and the specified window width w the lens flare window is defined as shown in Figure 3 to extract the lens flares from. Within this image subset we apply adaptive thresholding to extract the bright spots which usually correspond to lens flares. To remove noise in the resulting binary image a morphological opening (erosion followed by dilation) filter is applied. For the remaining shapes we calculate the center points where we fit a line to calculate the resulting flare direction α_{new}. If $|\alpha - \alpha_{new}|$ exceeds α_{thr}, an iterative refinement step is calculated as shown in Figure 7. The optional refinement loop allows correcting for errors in the initial lens flare direction estimate. Main reasons for errors are the rotation matrices

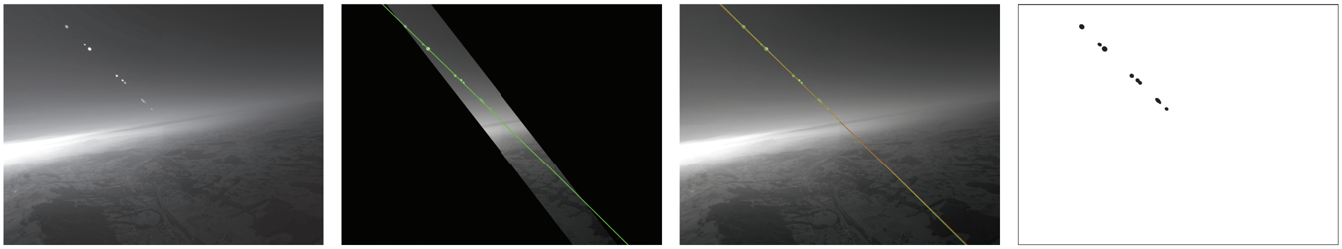

(a) Image source (b) Estimated lens flare direction (c) Refined lens flare direction (d) Resulting lens flare mask

Fig. 6. Overview of the different steps to detect lens flares. For illustration we chose a frame with inaccurate initial α. Based on the input frame (a) and the initial α the lens flare window is defined and potential lens flare candidates are extracted. A line is fitted through these lens flare candidates resulting in a new direction estimate α_{new}. If α and α_{new} are close, the final lens flares are extracted. Otherwise another refinement loop is calculated as explained in Section II-B. The final lens flares including the estimated direction are shown in (c). The detected lens flares are saved as a mask (d) which is used within the aerial object tracking framework. This figure is best viewed in color.

procedure DETECTLENSFLARES
    get α from sun position
    repeat
        set lens flare window given α and w
        get lens flare candidates
        fit line through lens flare candidates
        update α from fitted line
    until convergence
    verify lens flare candidates
    return detected lens flares
end procedure

Fig. 7. Basic algorithm to extract lens flares from an image.

R_{BN} and R_{CB} given by the attitude angles from the IMU and the extrinsic camera calibration, respectively. If the initial guess is purely based on image data, the minimal initial lens flare direction error is directly related to the step size $\Delta\alpha$. As long as the required meta information is available, the algorithm usually converges after 1-2 iterations.

To avoid declaring an approaching traffic aircraft within the lens flare window as a lens flare we require a consistent motion of the candidates together with the lens flare direction over multiple time steps. False detections of lens flares are further reduced by removing candidates which are not close to the final lens flare direction α. From the detected flares a filter mask is constructed as shown in Figure 6(d), to suppress those detections from playing a role in the aerial object tracking. The final algorithm for extracting lens flares from an aerial image in pseudo code is shown in Figure 7.

III. EVALUATING THE LENS FLARE DETECTION

This section focuses on the evaluation of our lens flare detection algorithm. After determining the optimal window width w, we present a detailed analysis of parameters and errors influencing the calculation of the lens flare direction.

A. Dataset and Performance Measurement

The key component to efficient lens flare detection is the accurate prediction of the lens flare direction α within the image. For a detailed analysis of parameters and errors influencing the lens flare direction we extracted 300 frames containing lens flares from the airborne imagery dataset. To evaluate the accuracy of the estimated α we manually labeled the correct lens flare direction α_{true} in all 300 images. As performance measurement for all the evaluations we are using the angular error:

$$\alpha_{err} = |\alpha_{estimate} - \alpha_{true}|. \tag{4}$$

As shown in Section II, the following parameters are required to calculate the initial lens flare direction α from the position of the sun:

- The lens flare window width w in pixels
- The current date and time in UTC
- The current observer position in WGS84 coordinates
- The current observer attitude (roll, pitch, yaw)

In the following we present the detailed evaluation of the parameters above. For every parameter we show the median of the angular error over all 300 images together with the 0.25, 0.75 and 0.95 quantiles.

B. Lens Flare Window Width w

First we determined the lens flare window width by evaluating different settings of w. The results are shown in Figure 8, where we show for every w the corresponding angular error across all 300 images. If the window width is chosen below 100 pixels, the angular error is significantly increasing. This is due to the fact that at some point the

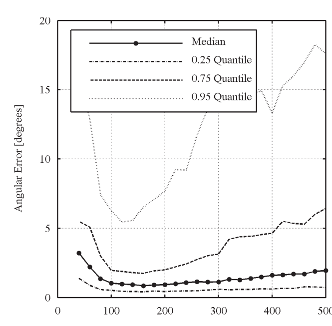

Fig. 8. Evaluation of the lens flare detection with different settings for the lens flare window width w. This allows us to identify w where the angular error is minimal at ~ 120 pixels for our camera setup.

lens flare window gets too narrow to contain the lens flares and correct for slight initial misalignment. Above about 200 pixels the error is also increasing which is primarily because of other parts in the image (e.g. bright clouds) which might get detected as lens flares and therefore the refinement will fail. With increasing w the computational costs are increasing as well. The chosen window width for our camera setup is at $w = 120$ pixels where the average angular error is minimal. The 0.95 quantile error of about 5° is due to various images with direct sunlight and blooming artifacts (see Figure 2). These large bright areas are affecting the accuracy of α in the refinement step even if the lens flares are correctly detected.

Note that all further evaluations of error influences such as date, time, position and attitude were calculated with a window width of 120 pixels.

C. Comparison of Lens Flare Direction Estimation Methods

In Section II-A we presented the calculation of the lens flare direction α from the sun position or with a pure image-based approach. In Figure 9(a) we show a direct comparison of these two approaches regarding their accuracy (angular error) across all 300 frames as box plots The angular error of the sun position based approach (on the left) is usually below $2 - 3^\circ$. In contrast, the image based approach (on the right) shows for some images outliers in the angular error of more than 20°. These frames usually contain overexposed clouds, heavy blooming or mountainous terrain with snow fields.

The computational cost of the image based approach is about ten times higher, as shown in Figure 9(b). This higher cost is primarily due to the multiple runs of the lens flare extraction to determine the most likely lens flare direction α. Nevertheless the image-based approach shows that we are still able to extract the correct lens flare angle in most situations without any additional information except the assumption of the direction going through the optical center of the image.

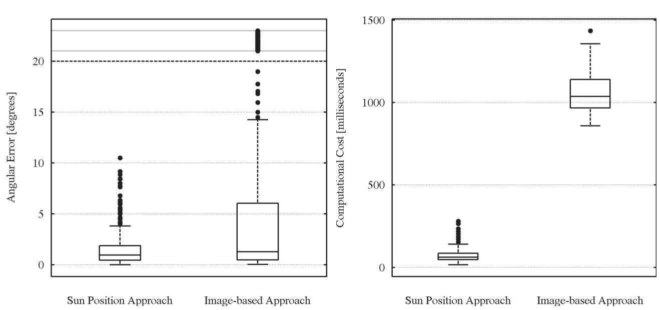

(a) Comparison of accuracy (b) Comparison of costs

Fig. 9. Comparison of the sun position based approach vs. the pure image based approach to calculate the lens flare direction α. Note that all frames with an accuracy error bigger than 20° are grouped together above the vertical line without maintaining the scaling of the vertical axis. The evaluation was computed with the following system configuration: Windows 7 x64, Intel Core i7-4800MQ, 16 GB RAM, Samsung SSD 840.

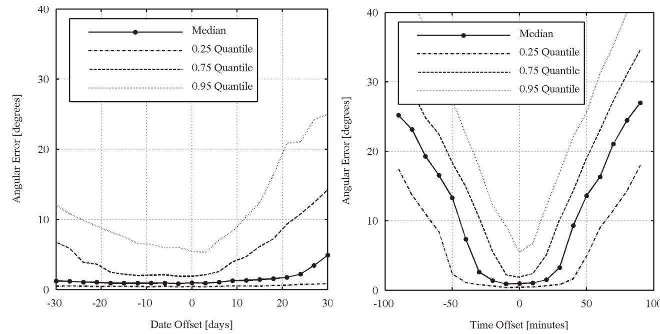

(a) Date error (b) Time error

Fig. 10. Overview of errors in the current date and time affecting the calculation of the lens flare direction α. The asymmetry in the date curve is a result of the season the images were recorded.

D. Errors Affecting the Lens Flare Direction

To calculate the lens flare direction α from the position of the sun we require the current date, time, position and attitude of the observer. In the following we show for each of these signals the influence of an error on the angular accuracy.

1) Error in date and time: As shown in Figure 10, an error in the current time is much more critical than an error in the current date. This is a very reasonable result because the ecliptic changes from day to day are very small. In contrast, the sun position changes during one day are significant.

2) Error in position: To analyze the influence of a position error we evaluated offsets in latitude and longitude direction in a range of $\pm 200\ km$. We can conclude that an error in position is rather irrelevant, because the resulting angular errors are in the range of $1.5 - 2^\circ$. Note that the same applies to an error in altitude.

3) Error in attitude: The most critical measurements for calculating a correct lens flare direction are the attitude angles, as shown in Figures 11(a) to 11(c). Due to our refinement loop we are able to compensate for attitude errors smaller than $\sim 3^\circ$. This allows us to fully correct inaccuracies in the IMU attitude angles including small delays during normal operation.

IV. Lens Flare Detection applied to Aerial Object Tracking

In order to suppress false tracks from lens flares we integrated the presented lens flare detection as additional filter step into the aerial object tracking framework. The extended pipeline is evaluated on scenarios with and without lens flares and we compare the results to those from the tracking framework without lens flare filter.

A. Extended Aerial Object Tracking Framework

The aerial object tracking framework shown in Figure 12 has as its main steps object detection, detection fusion and tracking. We use meta information from a GPS receiver, an IMU and a digital terrain model (DTM) to reduce false tracks due to ground clutter or static objects in the scene (e.g. dirt on the lens). The final results of the framework evaluation

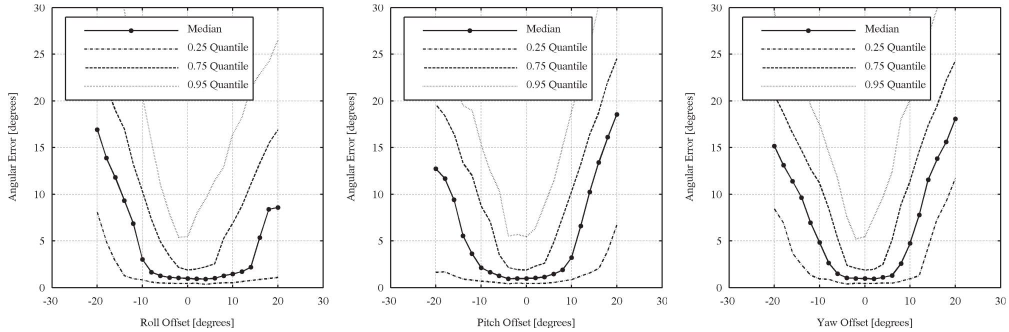

(a) Attitude error in roll (b) Attitude error in pitch (c) Attitude error in yaw

Fig. 11. Overview of errors in the attitude angles affecting the calculation of the lens flare direction α. These errors are the most critical ones in the calculation of the lens flare direction. Thanks to the iterative refinement within the estimation of the lens flare direction α we are able to successfully compensate for attitude errors up to $\sim 3^{\circ}$.

presented in [7] are shown in the middle of Table I, where the initial distance for having a valid track of the traffic aircraft, the corresponding remaining time to collision (TTC) and the total number of false tracks are presented. Note that the remaining time to collision is defined as the time from having a valid track until the time of the closest point of approach (CPA) in between both aircraft.

The framework is based on two detectors, the first uses morphological filters and the second builds upon an image differencing pipeline. Both of them suffer from the problem of detecting lens flares as potential traffic aircraft. The morphological detector - which is only applied within the sky region of the image - is tuned to detect black or white blobs, the latter unfortunately also a property of lens flares. The image differencing detector would not detect lens flares if their position is static within the image and the brightness is constant, but the camera system is mounted on an aerial platform where small motions of the camera continuously result in slightly changing positions or illumination levels of the lens flares. The higher the contrast of lens flares compared to the background the higher the response in the image differencing will be. Because of the similar trajectories of some lens flares compared to a correctly detected aircraft they cannot be removed by the existing filter pipeline (see Figures 13 and 14 for examples).

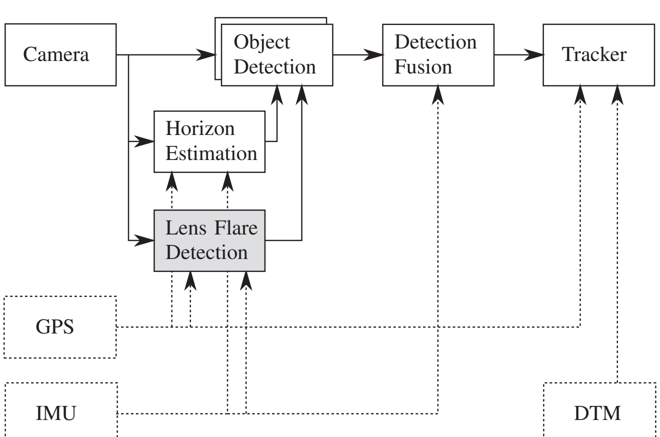

Fig. 12. System architecture of the aerial object tracking framework presented in [7], extended with the lens flare detection shown as gray box.

To remove false detections due to lens flares we have extended the existing tracking framework with an additional filter at the object detection stage. To that end we integrate the lens flare detection as a pre-processing step before running the detectors, shown as gray box in Figure 12. Once the positions of the lens flares are known, we use the corresponding lens flare mask to remove false detections and improve the overall signal to noise ratio. The detection fusion and tracking steps of the pipeline remain as-is.

B. Results

We evaluated the extended aerial object tracking framework on the existing *Scenarios A-K*. The results are shown on the right of Table I in direct comparison with the original results. Scenarios containing false tracks due to lens flares are visualized with a gray background. Except for *Scenario H*, we achieve the exact same results which prove that the removing of detections at lens flare positions does not degrade the performance of the existing tracking pipeline. Note that the high number of false tracks in *Scenario D* is due to a wrong assignment of detections to tracks which is not the focus of this paper.

Scenario H is the only one from the original dataset with a high number of false tracks due to lens flares. A direct comparison of example frames at four different time steps with disabled and enabled lens flare filter is presented in Figure 13. As results show, we are able to successfully suppress these false tracks. An interesting point is that we are even able to slightly increase the initial distance and corresponding TTC compared to the original results. This is a result of the tight integration of the lens flare filter within the detectors. By removing the high contrast lens flares before object detection, the signal to noise ratio within the image differencing detector is considerably improved and therefore the traffic aircraft is detected earlier. In Figure 13 this is observable by the longer track history (black) of the correctly tracked aircraft in the first frame with enabled lens flare filter (bottom row) compared to the frame without lens flare detection (top row).

TABLE I

EVALUATION OF THE AERIAL OBJECT TRACKING FRAMEWORK WITH AND WITHOUT LENS FLARE FILTER

	Scenarios from [7]		**Results from [7]**			**Results with lens flare filter**		
	Type	Background	Distance	TTC	False Tracks	Distance	TTC	False Tracks
A	Head-on	Sky	1874 m	17.6 s	1	1874 m	17.6 s	1
B	Head-on	Sky	1622 m	14.5 s	0	1622 m	14.5 s	0
C	Head-on	Terrain	980 m	7.8 s	0	980 m	7.8 s	0
D	Head-on	Terrain	1116 m	9.0 s	11	1116 m	9.0 s	11
E	Crossing	Sky	2830 m	35.3 s	2	2830 m	35.3 s	2
F	Crossing	Sky	2588 m	42.2 s	0	2588 m	42.2 s	0
G	Crossing	Sky	1831 m	17.7 s	2	1831 m	17.7 s	2
H	Crossing	Terrain	1550 m	14.2 s	18	1637 m	15.2 s	1
I	Crossing	Terrain	1489 m	14.0 s	2	1489 m	14.0 s	2
K	Crossing	Terrain	1593 m	23.4 s	4	1593 m	23.4 s	4
	Additional scenarios		**Results without lens flare filter**			**Results with lens flare filter**		
L	Crossing	Terrain	2884 m	39.6 s	5	2884 m	39.6 s	0
M	Head-on	Terrain	1419 m	11.0 s	5	1419 m	11.0 s	0
Average	-	-	1815 m	20.5 s	4	1822 m	20.6 s	2

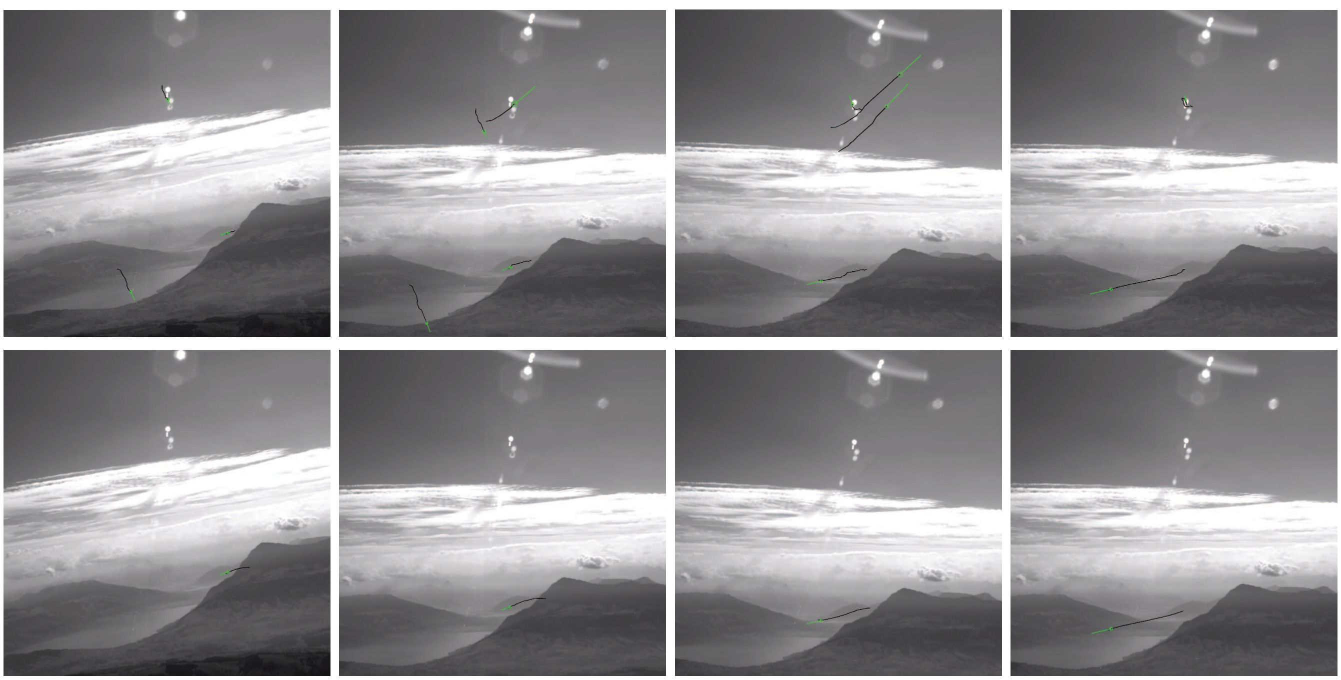

Fig. 13. Example frames from Scenario H at four consecutive time steps showing the detected tracks with their prediction over one second in green and the track history in black. The top row shows the results from the aerial object tracking framework without lens flare filter. Due to the egomotion of the aircraft multiple false tracks are spawned at lens flare positions. The bottom row shows the corresponding results with our lens flare detection integrated into the tracking framework, which allows for the successful removal of all false tracks from lens flares. This figure is best viewed magnified and in color.

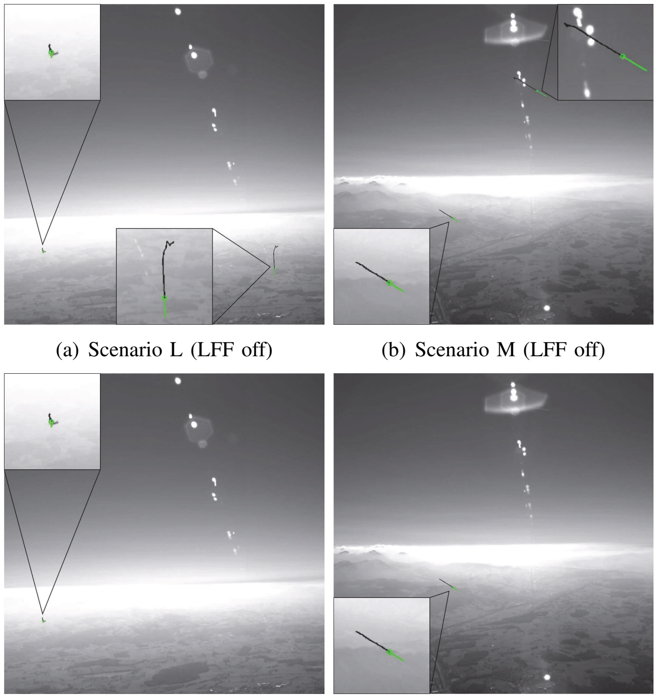

(a) Scenario L (LFF off) (b) Scenario M (LFF off)

(c) Scenario L (LFF on) (d) Scenario M (LFF on)

Fig. 14. Example images from Scenario L and M with disabled (LFF off) and enabled lens flare filter (LFF on) showing the detected tracks with the prediction over one second in green and the track history in black. The bottom row shows the correctly tracked traffic aircraft whereas in the top row there are also false tracks. Note the similar trajectories of false tracks and the traffic aircraft (best viewed in color).

For the verification of the results obtained with the original *Scenarios A-K* we evaluated two more scenarios that contain heavy lens flares with the enhanced aerial object tracking framework. At the bottom of Table I results are presented for the framework with disabled and enabled lens flare filter. With the original setup, false tracks due to lens flares are generated in both scenarios. The lower number of false tracks compared to *Scneario H* is a result of the aircraft egomotion. In *Scenario L and M* the own-ship is in level flight, whereas in *Scenario H* the pilot commands multiple small heading corrections. These heading corrections also affect the bank angle of the aircraft which has a direct impact on the lens flare direction within the cameras. As a result of the continuously changing lens flare direction the lens flares smoothly move around in the image and spawn multiple false tracks in *Scenario H* as shown in Figure 13. In any case, enabling the lens flare filter removed the false tracks in all scenarios tested. Example images from the tracker output from *Scenario L and M* are shown in Figure 14.

V. CONCLUSIONS

We presented a new two-step method to efficiently detect lens flares within aerial images based on the assumption that they are close to a line from the sun position through the optical center of the image. If the calculation of the lens flare direction from the sun position fails, we introduced a purely image based fallback solution. With a detailed analysis of signal errors affecting the calculation of the lens flare direction we outline the required precision of the additional meta information from the observer such as date, time, position and attitude. Experiments show that with the proposed method we usually achieve a final angular error in the lens flare direction of less than two degrees which is sufficiently accurate to extract the lens flares. We integrated the proposed lens flare detection into the aerial object tracking framework and evaluated the extended pipeline on existing and additional example scenarios with and without lens flares. As results show, the extension of the aerial object tracking framework with the additional lens flare filter does not degrade the tracking performance on scenarios without lens flares but successfully removes all false tracks due to lens flares.

REFERENCES

[1] Federal Aviation Administration, “Integration of civil unmanned aircraft systems (UAS) in the national airspace system (NAS) roadmap,” 2013.

[2] European Commission, “Roadmap for the integration of civil remotely-piloted aircraft systems into the european aviation system,” 2013.

[3] J. Utt, J. McCalmont, and M. Deschenes, “Test and integration of a detect and avoid system,” in *Proc. of AIAA ”Unmanned Unlimited” Technical Conference*, 2004.

[4] R. Carnie, R. Walker, and P. Corke, “Image processing algorithms for UAV ”sense and avoid”,” in *Proc. of International Conference on Robotics and Automation*, 2006.

[5] D. Dey, C. Geyer, S. Singh, and M. Digioia, “A cascaded method to detect aircraft in video imagery,” *International Journal of Robotics Research*, vol. 30, pp. 1527–1540, 2011.

[6] L. Mejias, J. S. Lai, and J. J. Ford, “Flight trial of an electro-optical sense-and-avoid system,” in *Proc. of International Congress of the Aeronautical Sciences*, 2012.

[7] A. Nussberger, H. Grabner, and L. Van Gool, “Aerial object tracking from an airborne platform,” in *Proc. of International Conference on Unmanned Aircraft Systems*, 2014.

[8] M. Owen, S. Duffy, and M. Edwards, “Unmanned aircraft sense and avoid radar: Surrogate flight testing performance evaluation,” in *Proc. of Radar Conference*, 2014.

[9] R. Kingslake, *Optics in Photography*, R. Kingslake, Ed. SPIE Optical Engineering Press, 1992.

[10] A. Gruen and T. S. Huang, *Calibration and Orientation of Cameras in Computer Vision*, A. Gruen and T. S. Huang, Eds. Springer Berlin Heidelberg, 2001.

[11] U.S. Naval Observatory and H.M. Nautical Almanac Office, “The astronomical almanac online,” http://asa.usno.navy.mil/, 2014.

[12] I. Reda and A. Andreas, “Solar position algorithm for solar radiation applications,” National Renewable Energy Laboratory, Tech. Rep., 2008.